Penta-graphene: A new carbon allotrope

Shunhong Zhang[a,b,c], Jian Zhou[c], Qian Wang[a,b,c,1], Xiaoshuang Chen[d,e], Yoshiyuki Kawazoe[f], and Puru Jena[c]

[a]Center for Applied Physics and Technology, College of Engineering, Peking University, Beijing 100871, China; [b]Collaborative Innovation Center of Inertial Fusion Sciences and Applications, Ministry of Education, Beijing 100871, China; [c]Department of Physics, Virginia Commonwealth University, Richmond, VA 23284; [d]National Laboratory for Infrared Physics, Shanghai Institute of Technical Physics, Chinese Academy of Sciences, Shanghai 200083, China; [e]Synergetic Innovation Center of Quantum Information & Quantum Physics, University of Science and Technology of China, Hefei, Anhui 230026, China; and [f]Institute for Materials Research, Tohoku University, Sendai, 980-8577, Japan

Edited by Ho-kwang Mao, Carnegie Institution of Washington, Washington, DC, and approved January 5, 2015 (received for review August 28, 2014)

A 2D metastable carbon allotrope, penta-graphene, composed entirely of carbon pentagons and resembling the Cairo pentagonal tiling, is proposed. State-of-the-art theoretical calculations confirm that the new carbon polymorph is not only dynamically and mechanically stable, but also can withstand temperatures as high as 1000 K. Due to its unique atomic configuration, penta-graphene has an unusual negative Poisson's ratio and ultrahigh ideal strength that can even outperform graphene. Furthermore, unlike graphene that needs to be functionalized for opening a band gap, penta-graphene possesses an intrinsic quasi-direct band gap as large as 3.25 eV, close to that of ZnO and GaN. Equally important, penta-graphene can be exfoliated from T12-carbon. When rolled up, it can form pentagon-based nanotubes which are semiconducting, regardless of their chirality. When stacked in different patterns, stable 3D twin structures of T12-carbon are generated with band gaps even larger than that of T12-carbon. The versatility of penta-graphene and its derivatives are expected to have broad applications in nanoelectronics and nanomechanics.

carbon allotrope | carbon pentagon | stability | negative Poisson's ratio | electronic structure

Carbon is one of the most versatile elements in the periodic table and forms a large number of allotropes ranging from the well-known graphite, diamond, C_{60} fullerene (1), nanotube (2), and graphene (3) to the newly discovered carbon nanocone (4), nanochain (5), graphdiyne (6), as well as 3D metallic structures (7, 8). The successful synthesis of graphene (3) has triggered considerable interest in exploring novel carbon-based nanomaterials. A wealth of 2D carbon allotropes beyond graphene has since been studied (see *SI Appendix*, Table S1 for details). Although some of these polymorphs such as graphdiyne (6) are metastable compared with graphene, they have been successfully synthesized. Moreover, some 2D carbon allotropes are predicted to exhibit remarkable properties that even outperform graphene, such as anisotropic Dirac cones (9), inherent ferromagnetism (10), high catalytic activity (6), and potential superconductivity related to the high density of states at the Fermi level (11). These results demonstrate that many of the novel properties of carbon allotropes are intimately related to the topological arrangement of carbon atoms and highlight the importance of structure–property relationships (12).

Pentagons and hexagons are two basic building blocks of carbon nanostructures. From zero-dimensional nanoflakes or nanorings (13) to 1D nanotube, 2D graphene, and 3D graphite and metallic carbon phases (7, 8), hexagon is the only building block. Extended carbon networks composed of only pentagons are rarely seen. Carbon pentagons are usually considered as topological defects or geometrical frustrations (14) as stated in the well-known "isolated pentagon rule" (IPR) (15) for fullerenes, where pentagons must be separated from each other by surrounding hexagons to reduce the steric stress. For instance, C_{60} consists of 12 pentagons separated by 20 hexagons forming the shape of a soccer ball, which is a perfect footnote to IPR. The emergence of carbon pentagons is also found to be accompanied by carbon heptagons in some cases (14), but are separated from each other. Inspired by the synthesis of pure pentagon-based C_{20} cage (16), considerable effort has been made to stabilize fused-pentagon-based and non-IPR carbon materials in various dimensionalities (10, 15). Some non-IPR fullerenes have been experimentally realized (15). A "pentagon-first" mechanism was postulated in the transformation from *sp* carbon chains to sp^2 carbon rings during surface growth of 2D carbon sheets (17). Thus, we conceived the idea of building 2D carbon sheets using fused pentagons as a structural motif. In this work, we show that a 2D carbon allotrope, penta-graphene, consisting entirely of pentagons, can indeed exist. The dynamical, thermal, and mechanical stability of this unique structure is confirmed by a series of state-of-the-art theoretical calculations. In addition, we show that pentagon-based carbon nanotubes, penta-tubes, formed by rolling up the penta-graphene sheet, and 3D twin structures of the recently reported T12-carbon (18) formed by stacking these sheets in different patterns, are both dynamically and thermally stable. We demonstrate that these exotic pentagon-based carbon materials exhibit interesting mechanical and electronic properties.

Results

Penta-Graphene Exfoliated from T12-Carbon. Our search for an all-pentagon-based 2D carbon sheet began by examining the recently proposed T12-carbon phase (18) that can be acquired by heating an interlocking-hexagon–based metastable carbon phase at high temperature (8). We note that there are two kinds of C–C bond lengths, namely, the slightly shorter intralayer bond (d_1) and the slightly longer interlayer bond (d_2), as shown in Fig. 1*A*. Here the atoms displayed in ball–stick model and highlighted in yellow form a layered structure which can be chemically

Significance

Carbon has many faces—from diamond and graphite to graphene, nanotube, and fullerenes. Whereas hexagons are the primary building blocks of many of these materials, except for C_{20} fullerene, carbon structures made exclusively of pentagons are not known. Because many of the exotic properties of carbon are associated with their unique structures, some fundamental questions arise: Is it possible to have materials made exclusively of carbon pentagons and if so will they be stable and have unusual properties? Based on extensive analyses and simulations we show that penta-graphene, composed of only carbon pentagons and resembling Cairo pentagonal tiling, is dynamically, thermally, and mechanically stable. It exhibits negative Poisson's ratio, a large band gap, and an ultrahigh mechanical strength.

Author contributions: Q.W. designed research; S.Z. and J.Z. performed research; S.Z., J.Z., Q.W., X.C., Y.K., and P.J. analyzed data; and S.Z., J.Z., Q.W., X.C., Y.K., and P.J. wrote the paper.

The authors declare no conflict of interest.

This article is a PNAS Direct Submission.

[1]To whom correspondence should be addressed. Email: qianwang2@pku.edu.cn.

This article contains supporting information online at www.pnas.org/lookup/suppl/doi:10.1073/pnas.1416591112/-/DCSupplemental.

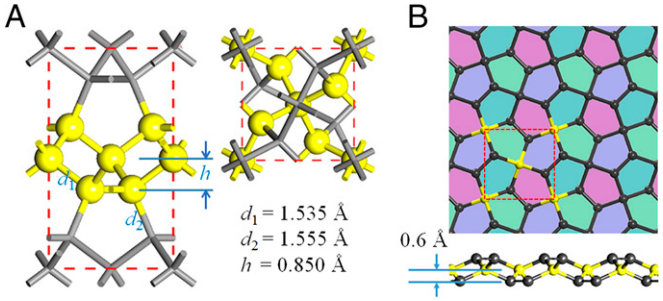

Fig. 1. (*A*) Crystal structure of T12-carbon viewed from the [100] and [001] directions, respectively. (*B*) Top and side views of the atomic configuration of penta-graphene. The square marked by red dashed lines denotes a unit cell, and the highlighted balls represent the sp^3 hybridized C atoms.

exfoliated from the T12-carbon phase. In fact, a monolayer can be fabricated from either a layered structure or a nonlayered structure (19). For van der Waals coupled layered structures like graphite, mechanical exfoliation (3) is sufficient to obtain the monolayer sheet (graphene), whereas for chemically bonded bulk phases like MAX (a family of transition metal carbides or nitrides), chemical exfoliation technique has been developed to extract a single layer (MXene) (20).

The optimized crystal structure of the 2D pentagon-based phase generated by exfoliating a single layer from T12-carbon is shown in Fig. 1*B*. The structure possesses $P\text{-}42_1m$ symmetry (space group no. 113) with a tetragonal lattice. The optimized lattice constants are $a = b = 3.64$ Å. The top view shows that the new phase is composed entirely of carbon pentagons, forming a beautiful pattern well known as Cairo pentagonal tiling (21). From the side view a buckling (0.6 Å) is observed, leading to a 2D sheet with a total thickness of 1.2 Å. This structure can be considered as a multidecker sandwich, with the 4-coordinated C atoms highlighted in yellow in Fig. 1*B* sandwiched between the 3-coordinated atoms. For convenience of discussion, we hereafter group the sp^3- and sp^2-hybridized C atoms as C1 and C2, respectively, and call this new graphene allotrope penta-graphene. The unit cell of penta-graphene contains six atoms as denoted by red dashed lines in Fig. 1*B* in which the C1 to C2 ratio is 1:2. The C1–C2 (1.55 Å) and C2–C2 (1.34 Å) bond lengths show pronounced characters of single and double bonds, respectively, and the bond angle $\theta_{C2\text{–}C1\text{–}C2}$ is 134.2°, indicating the distorted sp^3 character of C1 atoms. Such bond multiplicity (22) of carbon, although absent in the well-known diamond, graphite and graphene, has been found in a number of carbon structures with different dimensionalities (6–8, 22, 23) and is of general chemical interest as it leads to intermediate valency (23). Interestingly, we note that penta-graphene resembles the structure of experimentally identified layered silver azide (AgN_3) (24). By replacing the N_3 moieties and Ag atoms with the triconnected C dimers and tetra-connected C atoms, respectively, the geometry of penta-graphene can be realized.

Energetic Stability. Total energy calculations are performed to investigate the thermodynamic stability of penta-graphene. Although this phase is metastable compared with graphene and previously reported 2D carbon allotropes (6, 11, 14) due to its violation of the IPR, it is more stable than some nanoporous carbon phases such as 3D T-carbon (25), 2D α-graphyne (6), and (3, 12)-carbon sheet (26) (Fig. 2*A*). We also note that penta-graphene is energetically preferable over some experimentally identified carbon nanostructures such as the smallest fullerene, C_{20} and the smallest carbon nanotube, implying that the 2D penta-graphene sheet could be synthesized. Although C_{20} cage and penta-graphene share the structural motif of fused pentagons, unlike the highly curved C_{20} cage where all of the C atoms exhibit distorted sp^2 hybridization leading to a large strain energy, in penta-graphene the onset of sp^3 hybridization lowers the curvature of fused carbon pentagons, thus partially releasing the strain.

Dynamic Stability. Next we study the lattice dynamics of penta-graphene by calculating its phonon dispersion. The results are presented in Fig. 2*B*. The absence of imaginary modes in the entire Brillouin zone confirms that penta-graphene is dynamically stable. Similar to the phonons of graphene (27, 28), there are three distinct acoustic modes in the phonon spectra of penta-graphene. The in-plane longitudinal and in-plane transverse modes have linear dispersion near the Γ point, whereas the out-of-plane (ZA) mode has quadratic dispersion when $\boldsymbol{q}$ approaches $\mathbf{0}$. The quadratic ZA mode in the long-wavelength region is closely associated with the bending rigidity and lattice heat capacity of the nanosheet, which is discussed in detail in *SI Appendix*, text S1. A remarkable phonon gap is observed in the phonon spectra. Detailed analysis of the atom-resolved phonon density of states (PhDOS) reveals that the double bonds between the sp^2 hybridized C2 atoms are predominant in the dispersionless high-frequency modes (Fig. 2*B*), which is quite similar to the phonon modes in earlier reported sp^2–sp^3 hybrid carbon structures (7, 8).

Thermal Stability. The thermal stability of penta-graphene is examined by performing ab initio molecular dynamics (AIMD) simulations using canonical ensemble. To reduce the constraint of periodic boundary condition and explore possible structure reconstruction, the 2D sheet is simulated by (4 × 4), (6 × 6), and ($4\sqrt{2} \times 4\sqrt{2}$) *R*45° supercells, respectively. After heating at room temperature (300 K) for 6 ps with a time step of 1 fs, no structure reconstruction is found to occur in all of the cases. Furthermore, we find that the penta-graphene sheet can withstand temperatures as high as 1,000 K, implying that this 2D

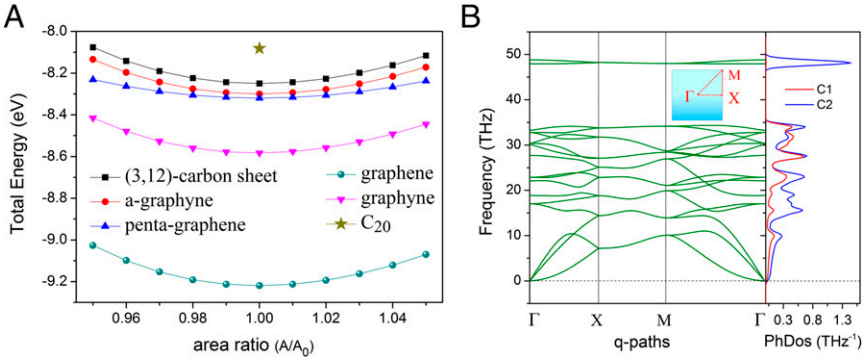

Fig. 2. (*A*) Area dependence of total energy per atom for some 2D carbon allotropes. The total energy of the experimentally identified dodecahedral C_{20} cage is also calculated and plotted here for comparison. (*B*) Phonon band structures and PhDOS of penta-graphene. (*Inset*) High-symmetric *q*-point paths: Γ (0, 0) → X (1/2, 0) → M (1/2, 1/2) → Γ (0, 0).

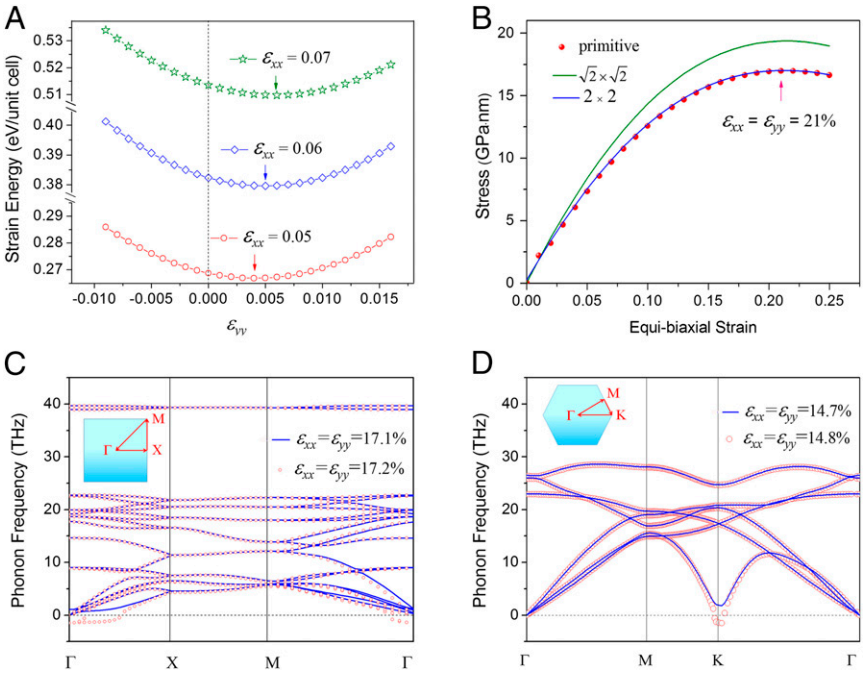

Fig. 3. (*A*) Strain energy with respect to the lateral lattice response when the penta-graphene lattice is under uniaxial strain along the *x* direction. The arrows indicate the equilibrium magnitude of ε_{yy}. (*B*) Stress–strain relationship under equi-biaxial tensile strain. The red arrow denotes the maximum strain. (*C*) Phonon bands of penta-graphene at the extreme of equi-biaxial strain. (*D*) Same as *C* for graphene. Blue lines and red circles represent phonons before and after the failure, respectively. (*Insets*) The high-symmetry *q*-point paths in the reciprocal space.

carbon phase is separated by high-energy barriers from other local minima on the potential energy surface (PES) of elemental carbon. The snapshots of atomic configurations of penta-graphene at the end of AIMD simulations are shown in *SI Appendix*, Fig. S1. The effect of point defects or rim atoms on the stability of the penta-graphene sheet is also studied by introducing mono- and di-vacancies, Stone–Wales-like defect, adatoms, and edge atoms. The results are presented in *SI Appendix*, text S2, Figs. S2–S4, where one can see that the stability and structure of penta-graphene is robust, despite the defects.

Mechanical Stability. As we fix the supercell during all of the MD simulations, it is necessary to assess the effect of lattice distortion on structural stability. To guarantee the positive-definiteness of strain energy following lattice distortion, the linear elastic constants of a stable crystal has to obey the Born–Huang criteria (29). We calculate the change of energy due to the in-plane strain to determine the mechanical stability of penta-graphene. For a 2D sheet, using the standard Voigt notation (26), i.e., 1-*xx*, 2-*yy*, and 6-*xy*, the elastic strain energy per unit area can be expressed as

$$U(\varepsilon)=\frac{1}{2}C_{11}\varepsilon_{xx}^2+\frac{1}{2}C_{22}\varepsilon_{yy}^2+C_{12}\varepsilon_{xx}\varepsilon_{yy}+2C_{66}\varepsilon_{xy}^2, \qquad [1]$$

where C_{11}, C_{22}, C_{12}, and C_{66} are components of the elastic modulus tensor, corresponding to second partial derivative of strain energy with respect to strain. The elastic constants can be derived by fitting the energy curves associated with uniaxial and equi-biaxial strains. The curves are plotted in *SI Appendix*, Fig. S5. For a mechanically stable 2D sheet (29), the elastic constants need to satisfy $C_{11}C_{22} - C_{12}^2 > 0$ and $C_{66} > 0$. Due to the tetragonal symmetry of penta-graphene, we have $C_{11} = C_{22}$. Thus, in this case we only need to satisfy $C_{11} > |C_{12}|$ and $C_{66} > 0$. Under uniaxial strain, $\varepsilon_{yy} = 0$, $U(\varepsilon) = 1/2C_{11}\varepsilon_{11}^2$. Parabolic fitting of the uniaxial strain curve yields $C_{11} = 265$ GPa·nm. Under equi-biaxial strain, $\varepsilon_{xx} = \varepsilon_{yy}$, we have $U(\varepsilon) = (C_{11} + C_{12})\varepsilon_{xx}^2$. Again, by fitting the equi-biaxial strain curve we obtain $C_{11} + C_{12} = 247$ GPa·nm, hence, $C_{12} = -18$ GPa·nm. Thus, the calculated elastic constants satisfy $C_{11} > |C_{12}|$, and the calculated C_{66} is positive, indicating that the 2D penta-graphene sheet is mechanically stable.

Mechanical Properties. Having confirmed the stability of penta-graphene, we next systematically study its mechanical properties. The in-plane Young's modulus, which can be derived from the elastic constants by $E = (C_{11}^2 - C_{12}^2)/C_{11}$, is calculated to be 263.8 GPa·nm, which is more than two-thirds of that of graphene (345 GPa·nm) (30) and is comparable to that of h-BN monolayer (26). Interestingly, we note that C_{12} is negative for this nanosheet, leading to a negative Poisson's ratio (NPR), viz., $\nu_{12} = \nu_{21} = C_{12}/C_{11} = -0.068$. To confirm this unusual result, we calculated the lateral response in the *y* direction when the lattice endures a tensile strain in the *x* direction. We examine cases with $\varepsilon_{xx} = 5\%$, 6%, and 7%. As expected, we find that the equilibrium lattice constant in the *y* direction is expanded in all of the cases (Fig. 3*A*). This confirms the NPR of penta-graphene. It is well known that Poisson's ratio is defined as the negative ratio of the transverse strain to the corresponding axial strain. Normally, this ratio is positive as most solids expand in the transverse direction when subjected to a uniaxial compression. Although the continuum mechanics theory does not rule out the possibility of emergence of NPR in a stable linear elastic material, it is fairly rare to find such NPR material in nature. However, it has been found that some artificial materials have NPR and exhibit excellent mechanical properties (31, 32). Such materials, usually referred to as auxetic materials or mechanical metamaterials, are of broad interest in both scientific and technological communities (33). Thus, penta-graphene with such unusual mechanical property may have multiple applications such as a tension activatable substrate, a nanoauxetic material, or a deformable variable-stiffness material.

Besides in-plane stiffness, ideal strength is also a very important mechanical property of a nanomaterial. We study the ideal strength of penta-graphene by calculating the variation of stress with equi-biaxial tensile strain using different cells. The results are plotted in Fig. 3*B*, which shows that the strain at the maximum stress is 21%. Such an ultrahigh ideal strength is exciting. However, we should note that phonon instability might occur before mechanical failure. Such failure mechanism has been well studied in graphene where the phonon softening induced by Kohn anomaly occurs before the stress reaches its maximum in the primitive cell (27, 28). To check whether similar phonon-

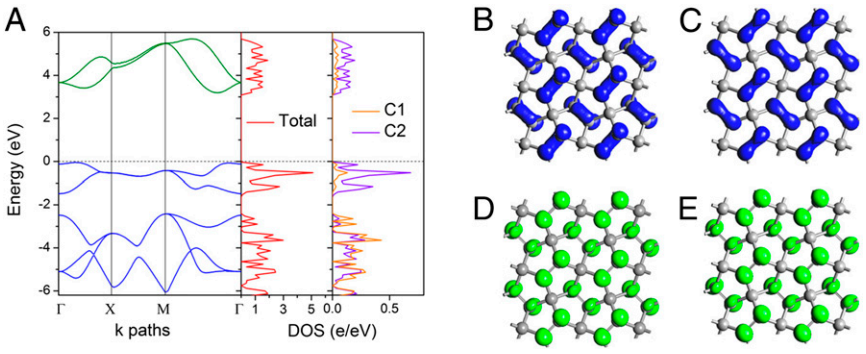

Fig. 4. (*A*) Electronic band structure and total and partial DOS of penta-graphene calculated by using HSE06 functional. The Fermi level is shifted to 0.00 eV. Band-decomposed charge density distributions are depicted in *B* to *E*: (*B*) the second highest occupied band, (*C*) the highest occupied band, (*D*) the lowest unoccupied band, and (*E*) the second lowest unoccupied band.

dominant failure mechanism exists in penta-graphene, we compute the phonons under increasing equi-biaxial strain. The results at the critical point of phonon softening are plotted in Fig. 3*C*. We find that phonon softening does not arise until the magnitude of equi-biaxial strain reaches 17.2%, which is smaller than the magnitude of 21% obtained from the stress–strain curve. For comparison, we also calculate phonons of the equi-biaxially stretched graphene. The observed softening of the K_1 mode at the Dirac point under equi-biaxial tensile strain of 14.8% (Fig. 3*D*) is in excellent agreement with previous work (27, 28). This indicates that the critical strain of penta-graphene is significantly larger than that of pristine graphene. It is also comparable to that of carrier-doping–strengthened graphene (28). At the critical strained state, the single bond lengths between C1 and C2 atoms reach ∼1.77 Å, which is comparable with the experimentally (34) and theoretically (35) reported longest C–C bond length. Detailed analyses on the eigenvectors corresponding to the imaginary modes reveal that the structure fracture stems from the breakdown of some of the σ bonds between C1 and C2 atoms.

Electronic Properties. To probe the electronic properties of penta-graphene, we calculate its band structure and corresponding total and partial density of states (DOS). As shown in Fig. 4*A*, penta-graphene is an indirect band-gap semiconductor with a band gap of 3.25 eV [computed using the Heyd–Scuseria–Ernzerhof (HSE06) functional] (36, 37), because the valance band maximum (VBM) lies on the Γ–X path whereas the conduction band minimum is located on the M–Γ path. However, due to the existence of the sub-VBM on the M-Γ path, which is very close to the true VBM in energy, penta-graphene can also be considered as a quasi-direct–band-gap semiconductor. Analysis of its partial DOS reveals that the electronic states near the Fermi level primarily originate from the sp^2 hybridized C2 atoms, which is further confirmed by calculating the band-decomposed charge density distributions, as shown in Fig. 4 *B*–*E*. A simplified tight-binding model is used to understand the underlying physics behind the band-gap opening feature in the band structure of penta-graphene (see *SI Appendix*, text S3 for details). We argue that it is the presence of the sp^3-hybridized C1 atoms that spatially separates the p_z orbitals of sp^2-hybridized C2 atoms, hindering full electron delocalization and thus giving rise to a finite band gap. The dispersionless, partially degenerate valance bands lead to a high total DOS near the Fermi level, lending to the possibility that Bardeen–Cooper–Schrieffer superconductivity can be achieved in this nanosheet through hole doping (38).

Penta-Tubes: Rolled-Up Penta-Graphene. It is well known that the electronic properties of carbon nanotubes are closely related to graphene according to the zone folding approximation (39). Due to the gapless semimetallic feature of graphene, the electronic properties of carbon nanotubes are highly chirality-dependent: a carbon nanotube is metallic only when its chiral vector (n, m) satisfies $n - m = 3l$, where l is an integer. The difficulty in fabricating and separating carbon nanotubes with certain conductance (metallic or semiconducting) greatly hinders its application in nanoelectronics. A previous study proposed a family of metallic carbon nanotubes based on metallic Heackelite sheet (11). It is therefore natural to expect that the penta-graphene–based nanotubes could be semiconducting regardless of chirality. To test this hypothesis we have constructed a series of pentagon-based carbon nanotubes by rolling up the penta-graphene sheet along the (n, m) chiral vectors, where $n = m$ range from 2 to 8 (Fig. 5*A*). The tubes with other chiralities ($n \neq m$) failed to converge to stable tubular structures. We name these pentagon-based carbon nanotubes penta-tubes. The optimized geometry of a (3, 3) penta-tube is illustrated in Fig. 5*B*. The dynamic and thermal stability of this nanotube is confirmed by carrying out phonon calculations and AIMD simulations, respectively. The results are presented in Fig. 5*C* and *SI Appendix*, Fig. S7, respectively. We find that not only all of the (n, n) penta-tubes are dynamically robust (*SI Appendix*, Fig. S8) but also they are thermally stable up to 1,000 K. Analysis of their band structures and DOS reveals that all of the stable penta-tubes are semiconducting. The calculated results are summarized in *SI Appendix*, Table S2. Except for the highly curved (2, 2) penta-tube, the band gaps of the (n, n) penta-tubes are not sensitive to their diameters. Thus, chirality-independent semiconducting carbon nanotubes can be produced for application in nanoelectronics. The semiconducting behavior of penta-tubes can be attributed to the electronic structure of penta-graphene, which resembles the case of other semiconducting monolayers such as h-BN monolayer and the corresponding nanotubes (40) which inherit the semiconducting feature.

3D Carbon Structures: Stacked Penta-Graphene Layers. To further explore the structural versatility of penta-graphene, we have

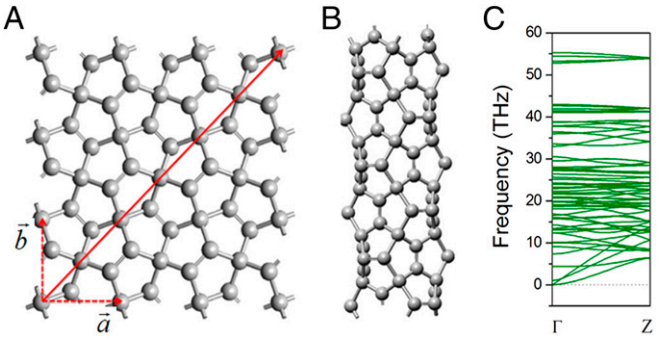

Fig. 5. (*A*) Illustration of chiral vectors of penta-tube. Dashed lines with arrows denote the lattice basis vector. (*B*) Optimized structure of (3, 3) penta-tube from side view, and (*C*) the corresponding phonon spectra.

PHYSICS

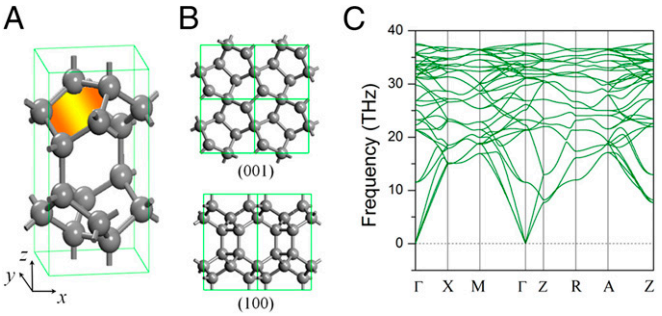

Fig. 6. (*A*) Crystal structure of AA-T12 carbon. (*B*) AA-T12 viewed from the [001] and [100] directions, and (*C*) the corresponding phonon spectra.

altered the stacking patterns of the penta-graphene layers, leading to a 3D structure as shown in Fig. 6 *A* and *B*. Following the nomenclature used to analyze the structural character of fused-pentagon-based Pentaheptite (14), we define the layer stacking in T12-carbon as AB type. The stacking of the designed structure shown in Fig. 6 *A* and *B* is then termed as AA type. It can be viewed as a twin structure of the T12-carbon phase. The calculated phonon spectra of AA-T12 are presented in Fig. 6*C*, confirming its dynamical stability. Indeed, more complicated structures are expected to be built, akin to the pentaheptite modification of graphene (14). An example of such structures containing four penta-graphene layers (24 atoms) per unit cell, termed ABAA-T24, is presented in *SI Appendix*, Fig. S9. The detailed structural information of these new 3D phases as well as T12-carbon, for comparison, is given in *SI Appendix*, Table S3. The calculated cohesive energies (averaged on each carbon atom) are −8.87, −8.92, and −8.98 eV for AA-T12, ABAA-T24, and T12-carbon, respectively, indicating that the AA-T12 and ABAA-T24 phases are nearly as stable as T12-carbon. Band structure calculations suggest that both AA-T12 and ABAA-T24 are semiconducting with the energy band gaps of 5.68 and 5.33 eV, respectively, which are even larger than that of T12-carbon (4.56 eV), indicating that these phases can be highly electrically resistant and optically transparent like those products of cold compressed graphite (41). The bulk moduli of these polymorphs are calculated by fitting the third-order Birch Murnaghan equation of states (42). Although the bulk moduli of AA-T12 (359 GPa) and ABAA-T24 (380 GPa) are slightly smaller than that of T12-carbon (403 GPa), they are comparable with that of cubic BN, suggesting their potential applications in machining. We note that a very recent theoretical work identified the AA-T12 structure by considering its Si analog (43). It is also pointed out that, like T12-carbon, AA-T12 is a universal structure shared by C, Si, Ge, and Sn, suggesting this family of tetragonal structures may be ubiquitous in elemental allotropes of group IVA elements.

Discussion

We have demonstrated via AIMD simulations that the metastable penta-graphene structure can withstand very high temperature. We note that the experimentally synthesized dodecahedral C_{20}, the smallest carbon fullerene consisting of only carbon pentagons, is metastable, but possesses outstanding thermal stability (up to 3,000 K) (44). These results imply that thermodynamic criteria may not be the deterministic factor in the synthesis of new carbon-based materials. In fact, due to the bonding versatility of carbon, the PES might be fairly complicated with numerous local minima (corresponding to metastable phases) separated from each other by considerable energy barriers. Graphite and cubic diamond are energetically superior to almost all other carbon polymorphs, namely, they correspond to the two lowest-lying valleys on the PES. The high-energy barrier between graphite and diamond makes it possible for both graphite and diamond to coexist in nature. However, recent experimental (41) and theoretical (45) advances have identified many intermediate phases between graphite and diamond during cold compression of graphite. Some of these phases are pressure-recovered, i.e., they can exist when the external pressure is removed. This stability is also ascribed to the considerable energy barrier. In fact, even in some surfaces of carbon structures, different structural reconstruction patterns are separated by appreciable kinetic energy barriers (35). These findings highlight the vital role that kinetics (22, 23) plays in carbon structure evolution, and fuel the exploration of new metastable carbon phases as functional materials.

We now reflect on the relationship between the special atomic configuration and exotic mechanical properties of penta-graphene. When the structure is under uniaxial tension, the expansive lateral response has two kinds of impact on the total energy: on one hand, it elongates the bond and weakens the binding energy; on the other hand, it significantly reduces the difference between the two lattice constants a and b, thus helping the structure to get close to its original tetragonal symmetry, reducing the bond distortion around the sp^3-bonded C1 atoms and lowering the strain energy. The structure thus evolves to its equilibrium as a result of compromise between these two competing factors. Detailed illustrations of atom evolution under uniaxial lattice stretch are presented in *SI Appendix*, text S4. Such regime is reminiscent of an earlier work (46) which argued that the combination of "chemical criteria" and "crystallographic criteria" in carbon materials can lead to exceptional mechanical properties. The ultrahigh critical strain of penta-graphene is also intimately related to its atomic structure. The buckled structure slows down the bond elongation and hence the structure is highly stretchable. Besides, graphene has topologically protected point-like Fermi surface, and the coupling between the electron states near the Fermi level and certain phonon mode leads to fast phonon softening under biaxial tension (27), whereas penta-graphene does not suffer from Kohn anomaly, because it is semiconducting.

One practical issue in the synthesis of penta-graphene is how to selectively break the interlayer covalent bonds in T12-carbon (18). To address this challenge, we point to a similar strategy where hydrogen intercalation was successfully used to decouple a graphene layer from the H–SiC (0001) surface (47, 48). Details of our exfoliation scheme are given in *SI Appendix*, text S5.

In summary, we showed that a 2D carbon sheet, penta-graphene, composed entirely of pentagons can be obtained by chemically exfoliating a single layer from the T12-carbon phase. Although penta-graphene is energetically metastable compared with graphene, it is dynamically stable and can withstand temperatures up to 1,000 K. Due to its special atomic configuration, penta-graphene has unusual properties, such as (*i*) it exhibits NPR, similar to that recently reported in a single-layer black phosphorus sheet (32); (*ii*) it exhibits ultrahigh ideal strength that can even outperform graphene; (*iii*) it is semiconducting, thus, there is no need to functionalize penta-graphene for opening the band gap as is the case with graphene. In addition, penta-graphene can be rolled up to form a 1D pentagon-based nanotube that is semiconducting regardless of its chirality. Therefore, there is no need to develop special techniques to separate semiconducting nanotubes from the metallic ones as is the case with conventional carbon nanotubes. Penta-graphene can also be stacked to form 3D stable structures displaying different properties from those of the mother-phase T12-carbon. Thus, penta-graphene sheet not only possesses exotic properties by itself but also can be used to build new structures. We hope that these findings will motivate experimental efforts. Once synthesized, these new carbon allotropes may not only enrich carbon science but also may lead to an untold number of applications.

Methods

First-principles calculations and AIMD simulations within the framework of density functional theory are performed using Vienna Ab initio Simulation Package (VASP) (49). The 2D system is separated from its periodic images by a vacuum distance of 20 Å in the perpendicular direction. Projector augmented wave (PAW) (50) method is used to treat interactions between ion cores and valance electrons. Plane waves with a kinetic energy cutoff of 500 eV are used to expand the valance electron ($2s^2 2p^2$) wavefunctions. The exchange-correlation potential is incorporated by using the generalized gradient approximation (51) due to Perdew–Burke–Ernzerhof in most of our calculations whereas a hybrid HSE06 (36, 37) functional is used for high-accuracy electronic structure calculations. The first Brillouin zone is represented by K points sampled using the Monkhorst–Pack scheme (52) with a grid density of $2\pi \times 0.02$ Å^{-1}. For geometry relaxation, the convergence thresholds for total energy and atomic force components are set at 10^{-4} eV and 10^{-3} eV Å^{-1}, respectively. In AIMD simulations the convergence criterion of total energy is set as 1 meV. Temperature control is achieved by Nosé thermostat (53). Structure relaxations are performed without any symmetry constraint. Phonon properties are calculated using finite displacement method implemented in Phonopy (54). A (4×4) supercell is constructed to calculate the atomic forces by using VASP, with a very high accuracy (stringent energy convergence criteria 10^{-8} eV per unit cell). Phonon calculations using a larger supercell (6×6) yield consistent results. For phonon calculations in graphene, an (8×8) supercell is used, which has been found in previous work (27) to be sufficient to take into account the long-range interatomic interactions.

ACKNOWLEDGMENTS. The authors thank the crew of the Center for Computational Materials Science, the Institute for Materials Research, Tohoku University (Japan), for their continuous support of the HITACHSR11000 supercomputing facility. This work is partially supported by grants from the National Natural Science Foundation of China (NSFC-51471004, NSFC-11174014, NSFC-10990104, and NSFC-11334008), the National Grand Fundamental Research 973 Program of China (Grant 2012CB921404), and the Doctoral Program of Higher Education of China (20130001110033). S.Z. acknowledges funding from the Graduate School of Peking University that enabled him to visit P.J.'s group at Virginia Commonwealth University, where the present work is partially conducted. P.J. acknowledges support of the US Department of Energy, Office of Basic Energy Sciences, Division of Materials Sciences and Engineering under Award DE-FG02-96ER45579.

1. Kroto HW, Heath JR, O'Brien SC, Curl RF, Smalley RE (1985) C_{60}: Buckminsterfullerene. *Nature* 318(6042):162–163.
2. Iijima S, Ichihashi T (1993) Single-shell carbon nanotubes of 1-nm diameter. *Nature* 363(6430):603–605.
3. Novoselov KS, et al. (2004) Electric field effect in atomically thin carbon films. *Science* 306(5696):666–669.
4. Charlier J-C, Rignanese G-M (2001) Electronic structure of carbon nanocones. *Phys Rev Lett* 86(26):5970–5973.
5. Jin C, Lan H, Peng L, Suenaga K, Iijima S (2009) Deriving carbon atomic chains from graphene. *Phys Rev Lett* 102(20):205501.
6. Li Y, Xu L, Liu H, Li Y (2014) Graphdiyne and graphyne: From theoretical predictions to practical construction. *Chem Soc Rev* 43(8):2572–2586.
7. Bucknum MJ, Hoffmann R (1994) A hypothetical dense 3,4-connected carbon net and related B_2C and CN_2 nets built from 1,4-cyclohexadienoid units. *J Am Chem Soc* 116(25):11456–11464.
8. Zhang S, Wang Q, Chen X, Jena P (2013) Stable three-dimensional metallic carbon with interlocking hexagons. *Proc Natl Acad Sci USA* 110(47):18809–18813.
9. Malko D, Neiss C, Viñes F, Görling A (2012) Competition for graphene: Graphynes with direction-dependent Dirac cones. *Phys Rev Lett* 108(8):086804.
10. Mina M, Susumu O (2013) Two-dimensional sp^2 carbon network of fused pentagons: All carbon ferromagnetic sheet. *Appl Phys Express* 6(9):095101.
11. Terrones H, et al. (2000) New metallic allotropes of planar and tubular carbon. *Phys Rev Lett* 84(8):1716–1719.
12. Xu L-C, et al. (2014) Two dimensional Dirac carbon allotropes from graphene. *Nanoscale* 6(2):1113–1118.
13. Omachi H, Nakayama T, Takahashi E, Segawa Y, Itami K (2013) Initiation of carbon nanotube growth by well-defined carbon nanorings. *Nat Chem* 5(7):572–576.
14. Deza M, Fowler PW, Shtogrin M, Vietze K (2000) Pentaheptite modifications of the graphite sheet. *J Chem Inf Comput Sci* 40(6):1325–1332.
15. Tan Y-Z, Xie S-Y, Huang R-B, Zheng L-S (2009) The stabilization of fused-pentagon fullerene molecules. *Nat Chem* 1(6):450–460.
16. Prinzbach H, et al. (2000) Gas-phase production and photoelectron spectroscopy of the smallest fullerene, C_{20}. *Nature* 407(6800):60–63.
17. Wang Y, et al. (2011) Template effect in the competition between Haeckelite and graphene growth on Ni(111): Quantum chemical molecular dynamics simulations. *J Am Chem Soc* 133(46):18837–18842.
18. Zhao Z, et al. (2012) Tetragonal allotrope of group 14 elements. *J Am Chem Soc* 134(30):12362–12365.
19. Naguib M, Gogotsi Y (2015) Synthesis of two-dimensional materials by selective extraction. *Acc Chem Res* 48(1):128–135.
20. Naguib M, et al. (2011) Two-dimensional nanocrystals produced by exfoliation of Ti_3AlC_2. *Adv Mater* 23(37):4248–4253.
21. Ressouche E, Simonet V, Canals B, Gospodinov M, Skumryev V (2009) Magnetic frustration in an iron-based Cairo pentagonal lattice. *Phys Rev Lett* 103(26):267204.
22. Menéndez-Proupin E, Montero-Alejo AL, García de la Vega JM (2012) Ultrathin carbon nanotube with single, double, and triple bonds. *Phys Rev Lett* 109(10):105501.
23. Merz KM, Hoffmann R, Balaban AT (1987) 3,4-connected carbon nets: Through-space and through-bond interactions in the solid state. *J Am Chem Soc* 109(22):6742–6751.
24. Schmidt CL, Dinnebier R, Wedig U, Jansen M (2007) Crystal structure and chemical bonding of the high-temperature phase of AgN_3. *Inorg Chem* 46(3):907–916.
25. Sheng X-L, Yan Q-B, Ye F, Zheng Q-R, Su G (2011) T-carbon: A novel carbon allotrope. *Phys Rev Lett* 106(15):155703.
26. Andrew RC, Mapasha RE, Ukpong AM, Chetty N (2012) Mechanical properties of graphene and boronitrene. *Phys Rev B* 85(12):125428.
27. Marianetti CA, Yevick HG (2010) Failure mechanisms of graphene under tension. *Phys Rev Lett* 105(24):245502.
28. Si C, Duan W, Liu Z, Liu F (2012) Electronic strengthening of graphene by charge doping. *Phys Rev Lett* 109(22):226802.
29. Ding Y, Wang Y (2013) Density functional theory study of the silicene-like SiX and XSi_3 (X = B, C, N, Al, P) honeycomb lattices: The various buckled structures and versatile electronic properties. *J Phys Chem C* 117(35):18266–18278.
30. Lee C, Wei X, Kysar JW, Hone J (2008) Measurement of the elastic properties and intrinsic strength of monolayer graphene. *Science* 321(5887):385–388.
31. Burns S (1987) Negative Poisson's ratio materials. *Science* 238(4826):551.
32. Jiang J-W, Park HS (2014) Negative Poisson's ratio in single-layer black phosphorus. *Nat Commun* 5:4727.
33. Greaves GN, Greer AL, Lakes RS, Rouxel T (2011) Poisson's ratio and modern materials. *Nat Mater* 10(11):823–837.
34. Schreiner PR, et al. (2011) Overcoming lability of extremely long alkane carbon-carbon bonds through dispersion forces. *Nature* 477(7364):308–311.
35. Lu S, Wang Y, Liu H, Miao MS, Ma Y (2014) Self-assembled ultrathin nanotubes on diamond (100) surface. *Nat Commun* 5:3666.
36. Heyd J, Scuseria GE, Ernzerhof M (2003) Hybrid functionals based on a screened Coulomb potential. *J Chem Phys* 118(18):8207–8215.
37. Heyd J, Scuseria GE, Ernzerhof M (2006) Erratum: "Hybrid functionals based on a screened Coulomb potential." *J Chem Phys* 124(21):219906.
38. Savini G, Ferrari AC, Giustino F (2010) First-principles prediction of doped graphane as a high-temperature electron-phonon superconductor. *Phys Rev Lett* 105(3):037002.
39. Charlier J-C, Blase X, Roche S (2007) Electronic and transport properties of nanotubes. *Rev Mod Phys* 79(2):677–732.
40. Ayala P, Arenal R, Loiseau A, Rubio A, Pichler T (2010) The physical and chemical properties of heteronanotubes. *Rev Mod Phys* 82(2):1843–1885.
41. Mao WL, et al. (2003) Bonding changes in compressed superhard graphite. *Science* 302(5644):425–427.
42. Murnaghan FD (1944) The compressibility of media under extreme pressures. *Proc Natl Acad Sci USA* 30(9):244–247.
43. Nguyen MC, Zhao X, Wang C-Z, Ho K-M (2014) sp^3-hybridized framework structure of group-14 elements discovered by genetic algorithm. *Phys Rev B* 89(18):184112.
44. Davydov IV, Podlivaev AI, Openov LA (2005) Anomalous thermal stability of metastable C_{20} fullerene. *Phys Solid State* 47(4):778–784.
45. Niu H, et al. (2012) Families of superhard crystalline carbon allotropes constructed via cold compression of graphite and nanotubes. *Phys Rev Lett* 108(13):135501.
46. Blase X, Gillet P, San Miguel A, Mélinon P (2004) Exceptional ideal strength of carbon clathrates. *Phys Rev Lett* 92(21):215505.
47. Riedl C, Coletti C, Iwasaki T, Zakharov AA, Starke U (2009) Quasi-free-standing epitaxial graphene on SiC obtained by hydrogen intercalation. *Phys Rev Lett* 103(24):246804.
48. Sołtys J, Piechota J, Ptasinska M, Krukowski S (2014) Hydrogen intercalation of single and multiple layer graphene synthesized on Si-terminated SiC(0001) surface. *J Appl Phys* 116(8):083502.
49. Kresse G, Furthmüller J (1996) Efficient iterative schemes for ab initio total-energy calculations using a plane-wave basis set. *Phys Rev B Condens Matter* 54(16):11169–11186.
50. Blöchl PE (1994) Projector augmented-wave method. *Phys Rev B Condens Matter* 50(24):17953–17979.
51. Perdew JP, Burke K, Ernzerhof M (1996) Generalized gradient approximation made simple. *Phys Rev Lett* 77(18):3865–3868.
52. Monkhorst HJ, Pack JD (1976) Special points for Brillouin-zone integrations. *Phys Rev B* 13(12):5188–5192.
53. Nosé S (1984) A unified formulation of the constant temperature molecular dynamics methods. *J Chem Phys* 81(1):511–519.
54. Togo A, Oba F, Tanaka I (2008) First-principles calculations of the ferroelastic transition between rutile-type and $CaCl_2$-type SiO_2 at high pressures. *Phys Rev B* 78(13):134106.

SI Appendix

Zhang et al.

SI Text

Text S1. Comparison of the ZA branch of penta-graphene and graphene

To quantitatively compare the ZA branch of graphene and penta-graphene, we first fit the long-wave relationship $\omega=cq^2$ (data points with a frequency lower than 80 cm^{-1} are used for fitting) to obtain the coefficient c. We fit the coefficient c of penta-graphene along the Γ-X and Γ-M directions, which are found to be 6.08×10^{-7} m^2s^{-1} and 5.82×10^{-7} m^2s^{-1}, respectively, exhibiting a slight anisotropy due to its tetragonal symmetry. The fitted c value for graphene is 5.40×10^{-7} m^2s^{-1}, which is in good agreement with previous result (1).

Quantitatively, the frequency-wave vector relationship, in the vicinity of the Γ point, can be formulated as: $\omega = cq^2 = \sqrt{D/\rho}q^2$ (2), where D and ρ correspond to the bending modulus and the mass area density of the nanosheet, respectively. We obtain the bending stiffness of graphene to be 1.36 eV, which is in good agreement with previous results (1, 3). Unlike graphene which has isotropic in-plane mechanical behavior due to the hexagonal symmetry, the ZA branch of penta-graphene shows direction-dependent dispersion and hence the bending rigidity is anisotropic. Our estimated bending moduli of penta-graphene along the axial and diagonal direction are 1.90 and 2.08 eV, respectively.

The ZA mode is also argued to be closely related to thermodynamic properties as it has the lowest vibrational energy among all modes and is most likely to be activated at low temperature.

Given the relationship $\omega = cq^2$ for the ZA mode, vibration density of states can be written as,

$$g(\omega) = \frac{S}{(2\pi)^2}\int \frac{dl}{|\nabla_q \omega(q)|} = \frac{S}{(2\pi)^2}\frac{2\pi q}{2cq} = \frac{S}{4\pi c}.$$

where S is the unit cell area. The Debye frequency ω_D can be determined by

$$N = \int_0^{\omega_D} g(\omega)d\omega = \frac{S\omega_D}{4\pi c}$$

Here N is the number of unit cells, and ω_D is the Debye frequency. In this case, the energy related to temperature can be written as

$$E(T)=\int_0^{\omega_D} g(\omega)\frac{\hbar\omega}{e^{\hbar\omega/k_BT}-1}d\omega=\frac{S}{4\pi c}\int_0^{\omega_D} k_BT\frac{\hbar\omega/k_BT}{e^{\hbar\omega/k_BT}-1}d\omega$$
$$=\frac{N(k_BT)^2}{k_B\theta_D}\int_0^{\frac{\theta_D}{T}}\frac{x}{e^x-1}dx=\frac{Nk_BT^2}{\theta_D}\int_0^{\frac{\theta_D}{T}}\frac{x}{e^x-1}dx,$$

here $\theta_D=\hbar\omega_D/k_B$ and $x=\hbar\omega/k_BT$.

The heat capacity contributed by the ZA mode can then be written as,

$$C_V^{ZA}(T)=\frac{\partial E}{\partial T}=\frac{\partial}{\partial T}\left(\frac{Nk_BT^2}{\theta_D}\int_0^{\frac{\theta_D}{T}}\frac{x}{e^x-1}dx\right).$$

At the low temperature limit, the integral goes from 0 to infinity. Considering

$$\int_0^{+\infty}\frac{x}{e^x-1}dx=\frac{\pi^2}{6},$$

we obtain

$$C_V^{ZA}(T)=\frac{N\pi^2k_B}{3}\frac{T}{\theta_D}=\frac{\pi k_B^{\,2}S}{12\hbar c}T,\qquad T\to 0.$$

Here we see that the ZA mode contributed heat capacity $C_V^{ZA}\sim T/c$ at low temperature. The calculated unit cell area for graphene and penta-graphene are 5.27 Å^2 and 13.25 Å^2, respectively, and with the fitted c values in hand, the ratio of C_V^{ZA}(penta-graphene)/ C^V_{ZA}(graphene) is calculated to be 2.3. This indicates that the ZA branch of penta-graphene contributes more to the heat capacity as compared to that of graphene.

Text S2. Stability of penta-graphene in the presence of defects

The defected penta-graphene is simulated by using a 4×4 supercell containing 96 atoms. The studied defects include monovacancies at the 4- and 3-coordinated C sites, respectively, the divacancy as missing a pair of the 3-coordinated C2 atoms, the Stone–Wales-like defect by rotating a pair of the 3-coordinated C2 atoms with an angle of 90 degrees, and the adatom by adding a C dimer at the two C2 sites crossing above another pair of C2 atoms, as shown in Fig. S2. The simulated STM images (under -1.0 V bias voltages) for the perfect as well as the divacancy defected penta-graphene are presented in Fig. S2C. We note that in such a supercell, defect concentration reaches 4.7×10^{17} cm^{-2}, significantly exceeding the experimentally observed vacancy concentration ($\sim3\times10^{11}$ cm^{-2}) in graphene (4). It is found, after full geometry optimization, that atomic structures of all the defected penta-graphenes are well sustained with almost the same buckling height (see the side views in Fig. S2). *Ab initio*

molecular dynamics simulations at 300 K are also carried out to confirm their thermal stability. The simulated results are given in Fig. S3 which shows that the integrity of the defected structures is still maintained after the systems are heated for five picoseconds (*ps*). No Domino effect appears and the total potential energies remain almost invariant. Therefore, the effect of the defects on the geometry of penta-graphene is "local". The structural stability as well as the thermal stability of the defected penta-graphene sheet suggests that penta-graphene is robust against defects as they can either partially release the stress or form more sp^3 hybridized C atoms.

The effect of edge atoms on the structural stability of penta-graphene is also considered by studying a penta-graphene nanoribbon. Our AIMD simulations (Fig. S4) indicate that the nanoribbon can withstand mild thermal perturbation at room temperature, which may be important for the synthesis.

Text S3. Discussion on the origin of finite band gap in penta-graphene

In graphene, all C atoms are sp^2-hybridized, thus each atom has an intact p_z orbital. These parallelly aligned p_z orbitals form delocalized states throughout the whole sheet, leading to two dispersive π and π* bands crossing at the Fermi level. The interactions of p_z orbitals, which is responsible for the gapless feature of graphene, can be described by a simple tight-binding Hamiltonian $H = -t\sum_{\langle i,j\rangle}\left(\hat{c}_i^{\dagger}\hat{c}_j + \text{H.c.}\right)$, with a constant hopping integral t. Introduction of sp^3-hybridized C atoms destroys the homogenously delocalized π and π* states and opens a band gap, as seen in graphane (5).

Our computed orbital-resolved PDOS and band decomposed charge density show that the frontier bands of penta-graphene are dominated by the p_z states of sp^2-hybridized C2 atoms. However, these orbitals are spatially separated by the sp^3-hybridized C1 atoms and full delocalization is hindered, resembling the case of graphane. We construct a modified tight-binding Hamiltonian to describe the interaction of these orbitals (Fig. S6A):

$$\hat{H} = -t\sum_{\langle i,j\rangle, i,j\in\{\text{C2}\}}\left(\hat{c}_i^{\dagger}\hat{c}_j + \text{H.c.}\right) - t'\sum_{\langle i,j\rangle, i\in\{\text{C2}\}, j\in\{\text{C1}\}}\left(\hat{d}_i^{\dagger}\hat{d}_j + \text{H.c.}\right),$$

where the parameter t denotes the hopping integral between the two C2-p_z orbital, t' is the hopping integral between a C2-p_z orbital and a C1-sp^3 orbital. $c_i^{\dagger}$ ($d_i^{\dagger}$) is the creation operator on the site i, and c_j (d_j) is the corresponding annihilation operator at site j.

We alter the t'/t ratio to examine the band evolution. Two typical cases are observed: when $t'=0.4t$, the gapped feature is observed in tight binding bands and the basic features of the DFT bands are qualitatively reproduced, whereas setting $t'=t$ leads to closing of the band gap (Fig. S6A). The former case can be easily understood as the overlap between two C2-p_z orbitals is obviously larger than that between a C2-p_z orbital and a C1-sp^3 orbital, considering their orientations. The calculated maximally localized Wannier Functions (MLWF) (6, 7) of penta-graphene projected onto certain atomic orbitals (Fig. S6B) shows an "asymmetric lobe" feature indicating that these orbitals are perturbed due to the imperfect sp^2 hybridization. To understand the underlying physics of the band gap closing in the $t'=t$ case, we need to alter the penta-graphene structure to enhance the C1-C2 hopping, to this end a hypothetical "flat penta-graphene (FPG)" model is constructed by compressing penta-graphene into a planar sheet. In this circumstance each planar tetra-coordinated C1 atom possesses an unhybridized p_z orbital (8), which is also confirmed by our calculated MLWFs (Fig. S6C). DFT calculation indicates FPG is metallic, consistent with the tight binding result with $t=t'$.

Based on the above mentioned results and analyses, we can conclude that it is the existence of sp^3-hybridized C1 atoms that hinders the full delocalization of C2 p_z orbitals, and the resultant localized states lead to less dispersive bands with a gap near the Fermi level.

Text S4. Illustration of the origin of NPR effect in penta-graphene

To illustrate the origin of NPR effect in penta-graphene we begin with a simple model, namely that of a methane molecule with T_d symmetry, plotted in the left panel of Fig. S10A. The $\bar{4}$ axis as well as the two mirror planes $m1$ and $m2$ are also displayed. We performed simple DFT calculations to study how the H atoms in the $m2$ plane respond when the atoms in the $m1$ plane suffer a distortion. If the $m1$ plane rotates along the $\bar{4}$ axis, H atoms in the $m2$ plane rotate adaptively to minimize Coulomb repulsion and damp the system from deviation from the T_d symmetry, as shown in the right panel of Fig. S10A. In penta-graphene, when the lattice endures uniaxial tension, the sp^2-hybridized C2 atoms evolve in a similar way. We assume that the central sp^3-hybridized C1 atom is fixed. When stretching the lattice, the C2 atoms, colored orange in Fig. S10B, move outward along the tensile direction, leading to a clockwise rotation of the $m1$ plane. Consequently, the $m2$ plane rotates in the same direction, resulting in an expansive lateral response to the lattice. Therefore, NPR effect is exhibited in

penta-graphene.

Text S5. A possible pathway to synthesize a monolayer penta-graphene

It has been demonstrated experimentally and theoretically that a graphene layer grown on SiC (0001) surface can be decoupled from the outermost Si layer by selectively breaking the covalent Si-C bonds using hydrogen intercalation (9, 10). Following this idea, we have simulated the effect of hydrogen intercalation in T12-carbon for obtaining a penta-graphene sheet.

To mimic the chemical exfoliation procedure in T12-carbon, we first computationally cleaved a (001) thin film from T12-carbon and carefully confirmed its structural stability via phonon calculation (Fig. S11A) and AIMD simulations. No surface reconstructions were found at 300 K, implying that the film can serve as a suitable precursor for chemical exfoliation. At the initial point, all hydrogen atoms existed in molecular form with nearly-uniform distribution and random orientation with the minimum C-H distance larger than 1.5 Å. When the system reached new equilibrium, a penta-graphene monolayer with partial hydrogenation is separated and lifted from the thin film surface (Fig. S11B). This process is quite similar to what happened in graphene-SiC (9, 10). Our simulations indicate that hydrogen intercalation may be a viable way to selectively break the interlayer C-C bonds in T12-carbon and to chemically exfoliate a penta-graphene monolayer. Penetration of hydrogen directly through the thin film surface may encounter high energy barriers like that in the case of graphene, but we note that such penetration may occur in the vicinity of local defects or grain boundaries (9). In a realistic situation the topmost carbon layers may also be hydrogenated by exposing to hydrogen atmosphere which may help to prevent the quasi freestanding sheet from folding. Subsequent dehydrogenation of penta-graphene may be achieved through annealing approach demonstrated in Ref (5).

1. Sánchez-Portal D, Artacho E, Soler JM, Rubio A, Ordejón P (1999) *Ab initio* structural, elastic, and vibrational properties of carbon nanotubes. *Phys Rev B* 59(19):12678-12688.
2. Muñoz E, Lu J, Yakobson BI (2010) Ballistic Thermal Conductance of Graphene Ribbons. *Nano Lett* 10(5):1652-1656.
3. Wei Y, Wang B, Wu J, Yang R, Dunn ML (2012) Bending Rigidity and Gaussian Bending Stiffness of Single-Layered Graphene. *Nano Lett* 13(1):26-30.
4. Ugeda MM, Brihuega I, Guinea F, Gómez-Rodríguez JM (2010) Missing Atom as a Source of Carbon Magnetism. *Phys Rev Lett* 104(9):096804.
5. Elias DC*, et al.* (2009) Control of Graphene's Properties by Reversible Hydrogenation: Evidence for Graphane. *Science* 323(5914):610-613.
6. Mostofi AA*, et al.* (2008) wannier90: A tool for obtaining maximally-localised Wannier functions. *Comput Phys Commun* 178(9):685-699.
7. Marzari N, Mostofi AA, Yates JR, Souza I, Vanderbilt D (2012) Maximally localized Wannier functions: Theory and applications. *Rev Mod Phys* 84(4):1419-1475.
8. Hoffmann R, Alder RW, Wilcox CF (1970) Planar tetracoordinate carbon. *J Am Chem Soc* 92(16):4992-4993.
9. Riedl C, Coletti C, Iwasaki T, Zakharov AA, Starke U (2009) Quasi-Free-Standing Epitaxial Graphene on SiC Obtained by Hydrogen Intercalation. *Phys Rev Lett* 103(24):246804.
10. Sołtys J, Piechota J, Ptasinska M, Krukowski S (2014) Hydrogen intercalation of single and multiple layer graphene synthesized on Si-terminated SiC(0001) surface. *J Appl Phys* 116(8):083502.

SI Tables

Table S1. Summary of the topological signatures and electronic properties of some currently identified two dimensional (2D) carbon allotropes, showing that hexagons are the primary building blocks of many of these materials, while carbon 2D structures made exclusively of pentagons are not known.

2D carbon structures	Carbon rings	Lattice [a]	Electronic property [b]
graphene (1)	6	H	D
Spirographite (2)	6	O	M
α-graphyne (3)	18	H	D
graphyne (4)	6+12	H	S
6,6,12-graphyne (3)	6+12	O	D
δ-graphyne (5)	6+14	H	D
β-graphyne (3)	12+18	H	D
Planar C_4 (6, 7) or T-graphene (8)	4+8	T	M
Pentaheptite (6, 9, 10)	5+7	M or O [c]	M
OPZ-L (6, 11)	5+8	M	M
OPZ-Z (6, 11)	5+8	O	G
Fused-pentagon network (12)	5+12	H	M
C_{31}-sheet (6, 13)	3+9	H	M
C_{41}-sheet (13)	4+7	T	M
C_{63}-sheet (13)	3+6+8	H	M
biphenylene (6, 14) or net-C (15)	4+6+8	O	M
H-net (16)	4+6+8	T	S
net-W (15, 17)	4+6+8	O	M
S-graphene (17)	4+6+10	O	D
BPC (13, 18) graphenylene((19)	4+6+12	H	S
pza-C_{10} (20)	5+6+7	M	S
Heackelite (21)	5+6+7	H or M	M
Dimerite (22)	5+6+7	H	M
Octite (23)	5+6+8	O	S
HOPG (24)	5+6+8	O	M
C_{65}-sheet (13)	5+6+9	H	M

[a] Considering the finite-thickness of some 2D carbon allotropes, we use 3D lattices wherein the *c* axis is perpendicular to the basal plane of the carbon sheets. The "H", "T", "O", and "M" represent hexagonal, tetragonal, orthogonal, and monoclinic, respectively.

[b] The "S" , "M", "G" and "D" represent semiconductor, metal, gapless semimetal, and Dirac semimetal, respectively. Dirac semimetal means that there exist Dirac cones near the Fermi level in the electronic band structure of the carbon sheet.

[c] Symmetry depends on the topological arrangements.

1. Novoselov KS*, et al.* (2004) Electric field effect in atomically thin carbon films. *Science* 306(5696):666-669.
2. Bucknum MJ, Hoffmann R (1994) A hypothetical dense 3,4-connected carbon net and related B_2C and CN_2 nets built from 1,4-cyclohexadienoid units. *J Am Chem Soc* 116(25):11456-11464.
3. Malko D, Neiss C, Viñes F, Görling A (2012) Competition for graphene: graphynes with direction-dependent Dirac cones. *Phys Rev Lett* 108(8):086804.
4. Narita N, Nagai S, Suzuki S, Nakao K (1998) Optimized geometries and electronic structures of graphyne and its family. *Phys Rev B* 58(16):11009-11014.
5. Zhao M, Dong W, Wang A (2013) Two-dimensional carbon topological insulators superior to graphene. *Sci Rep* 3:3532.
6. Merz KM, Hoffmann R, Balaban AT (1987) 3,4-connected carbon nets: through-space and through-bond interactions in the solid state. *J Am Chem Soc* 109(22):6742-6751.
7. Enyashin AN, Ivanovskii AL (2011) Graphene allotropes. *Phys Status Solidi B* 248(8):1879-1883.
8. Liu Y, Wang G, Huang Q, Guo L, Chen X (2012) Structural and electronic properties of T-Graphene: a two-dimensional carbon allotrope with tetrarings. *Phys Rev Lett* 108(22):225505.
9. Crespi VH, Benedict LX, Cohen ML, Louie SG (1996) Prediction of a pure-carbon planar covalent metal. *Phys Rev B* 53(20):R13303-R13305.
10. Deza M, Fowler PW, Shtogrin M, Vietze K (2000) Pentaheptite modifications of the graphite sheet. *J Chem Inf Comp Sci* 40(6):1325-1332.
11. Su C, Jiang H, Feng J (2013) Two-dimensional carbon allotrope with strong electronic anisotropy. *Phys Rev B* 87(7):075453.
12. Mina M, Susumu O (2013) Two-dimensional sp^2 carbon network of fused pentagons: all carbon ferromagnetic sheet. *Appl Phys Express* 6(9):095101.
13. Lu H, Li S-D (2013) Two-dimensional carbon allotropes from graphene to graphyne. *J Mater Chem C* 1(23):3677-3680.
14. Hudspeth MA, Whitman BW, Barone V, Peralta JE (2010) Electronic properties of the Biphenylene sheet and its one-dimensional derivatives. *ACS Nano* 4(8):4565-4570.
15. Wang X-Q, Li H-D, Wang J-T (2013) Prediction of a new two-dimensional metallic carbon allotrope. *Phys Chem Chem Phys* 15(6):2024-2030.
16. Hu M*, et al.* (2014) Theoretical two-atom thick semiconducting carbon sheet. *Phys Chem Chem Phys*.
17. Xu LC*, et al.* (2014) Two dimensional Dirac carbon allotropes from graphene. *Nanoscale* 6(2):1113-1118.
18. Brunetto G*, et al.* (2012) Nonzero gap two-dimensional carbon allotrope from porous graphene. *J Phys Chem C* 116(23):12810-12813.

19. Song Q*, et al.* (2013) Graphenylene, a unique two-dimensional carbon network with nondelocalized cyclohexatriene units. *J Mater Chem C* 1(1):38-41.
20. Luo X*, et al.* (2012) Two-dimensional superlattice: modulation of band gaps in graphene-based monolayer carbon superlattices. *J Phys Chem Lett* 3(22):3373-3378.
21. Terrones H*, et al.* (2000) New metallic allotropes of planar and tubular carbon. *Phys Rev Lett* 84(8):1716-1719.
22. Lusk MT, Carr LD (2009) Creation of graphene allotropes using patterned defects. *Carbon* 47(9):2226-2232.
23. Appelhans DJ, Lin Z, Lusk MT (2010) Two-dimensional carbon semiconductor: density functional theory calculations. *Phys Rev B* 82(7):073410.
24. Mandal B, Sarkar S, Pramanik A, Sarkar P (2013) Theoretical prediction of a new two-dimensional carbon allotrope and NDR behaviour of its one-dimensional derivatives. *Phys Chem Chem Phys* 15(48):21001-21006.

Table S2. Diameter (d) and band gap (E_g) at the GGA/PBE level for the (n, n) penta-tubes.

n	2	3	4	5	6	7	8
d (Å)	3.559	5.089	6.734	8.354	9.979	11.609	13.328
E_g (eV)	1.783	2.399	2.540	2.608	2.514	2.474	2.334

Table S3. Structural parameters of the tetragonal T12-carbon phase and its counterparts derived from the penta-graphene sheet.

Structure	Space group	Lattice parameters	Wyckoff Atomic Positions
T12	$P4_2/ncm$ (138)	a = 3.43 Å c = 6.09 Å	8*i* (0.3319, 0.8319, 0.3597) 4*b* (0, 0, 0)
AA-T12	$P4_2/mnm$ (136)	a = 3.52 Å c = 6.29 Å	4*d* (0, 1/2, 1/4) 8*j* (0.8451, 0.8451, 0.6244)
ABAA-T24	$P\text{-}42_1m$ (113)	a = 3.48 Å c =12.39 Å	2*a* (0, 0, 0) 2*b* (0, 0, 1/2) 4*e* (0.8316, 0.3316, 0.0686) 4*e* (0.3435, 0.8435, 0.5645) 4*e* (0.3330, 0.8330, 0.1762) 4*e* (0.8426, 0.6573, 0.3093) 4*d* (0.5000, 0.5000, 0.2454)

SI Figures

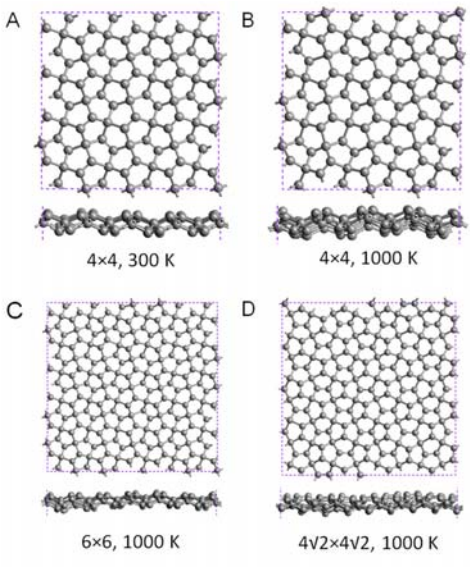

Fig. S1. Snapshots of atomic configurations of penta-graphene at the end of AIMD simulations. The simulated supercells are marked by purple squares, and their corresponding size and temperature are denoted below the each panel.

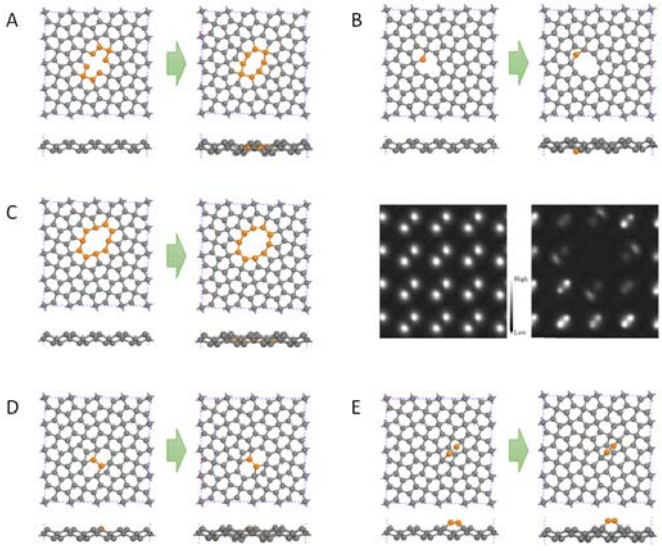

Fig. S2. Typical local defects in penta-graphene: (A) a monovacancy at the 4-coordinated C1 site; (B) a monovacancy at the 3-coordinated C2 site; (C) a divacancy by removing a pair of 3-coordinated C2 atoms and the simulated STM images before and after the defect is formed; (D) the Stone–Wales-like defect; and (E) an added C dimer. Both the initial and optimized atomic structures are displayed in the top and side views, with the atoms involved in local distortion marked in orange.

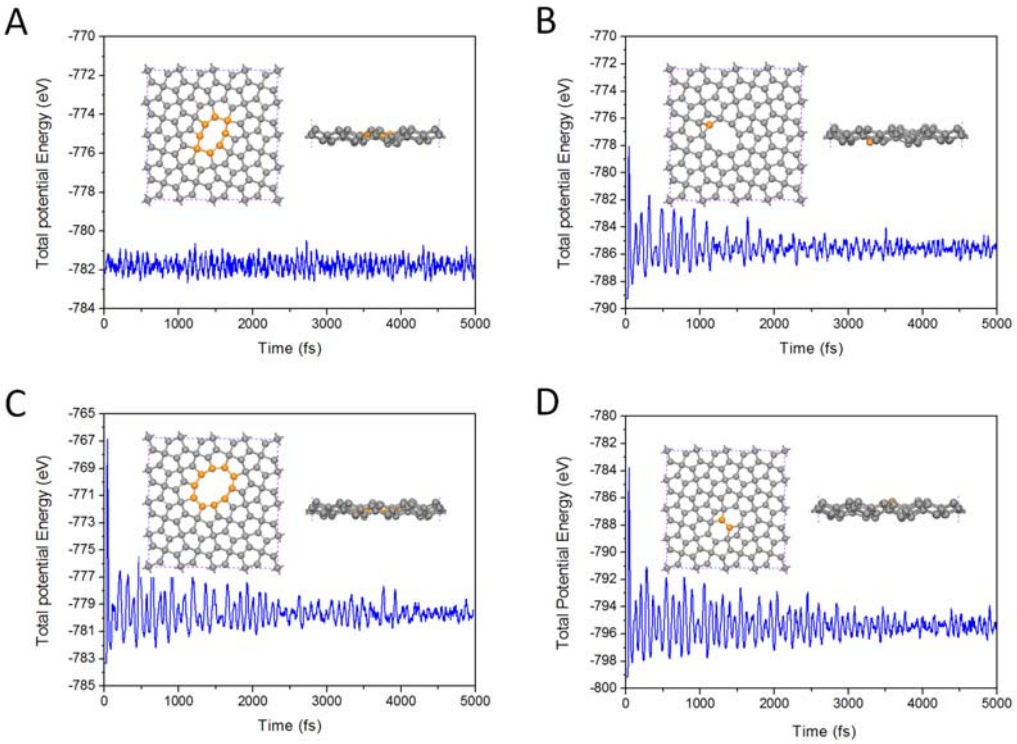

Fig. S3. Total potential energy fluctuation during AIMD simulations of penta-graphene with the defects: (A) a monovacancy at the C1 site; (B) a monovacancy at the C2 site; (C) a divacancy by removing a pair of C2 atoms; (D) the Stone–Wales-like defect. The insets show the snapshot at 5 *ps* for each simulation.

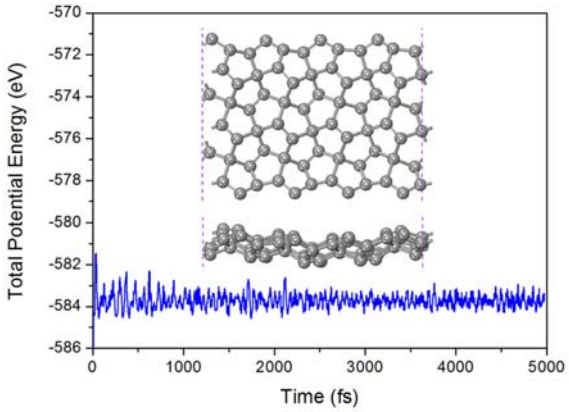

Fig. S4. Total potential energy fluctuation of a penta-graphene nanoribbon during AIMD simulations at 300 K. The inset shows the snapshot at the end of simulation, with purple dashed lines denoting the unit cell in the periodic direction.

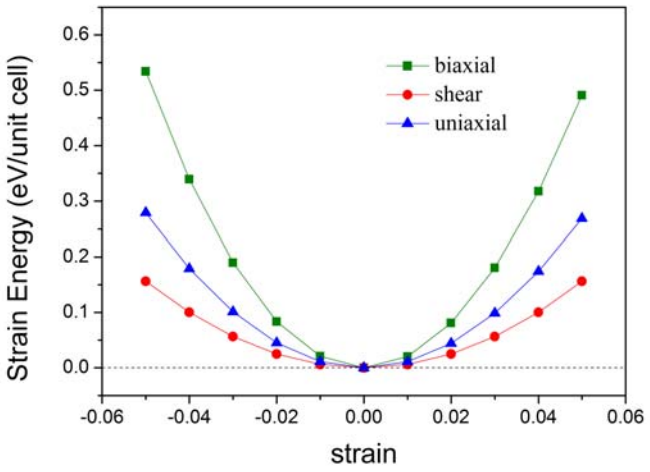

Fig. S5. Strain energy of penta-graphene under different kinds of in-plane strain. Note that the uniaxial strain curve is calculated by intentionally fixing the lateral lattice constant so that the strain energy can be simplified into the form $U(\varepsilon)=\frac{1}{2}C_{11}\varepsilon_{xx}^2$.

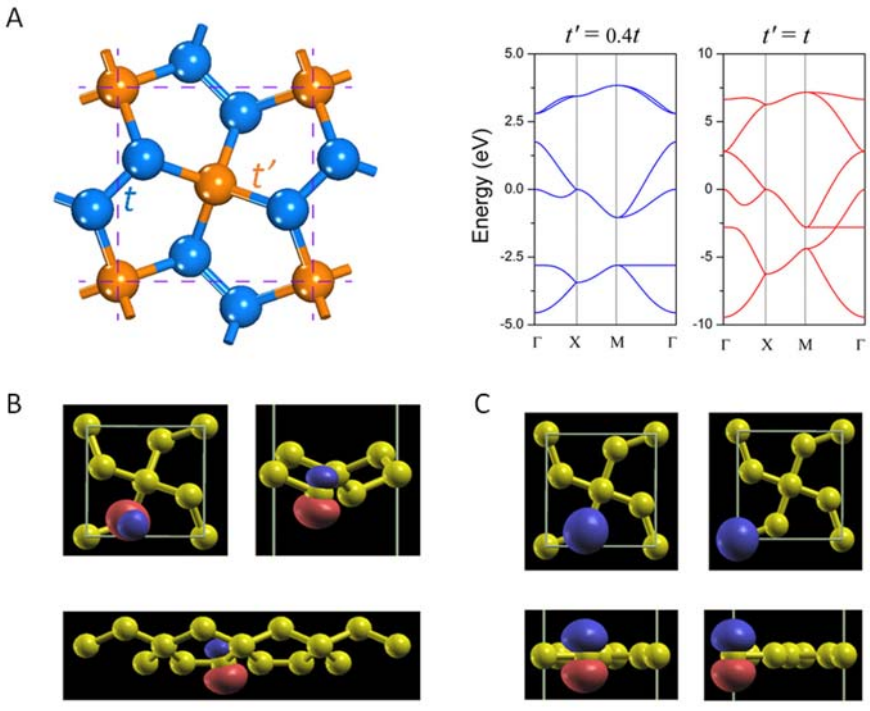

Fig. S6. (A) Illustration of hopping in the tight binding model and the corresponding bands with t'=0.4t and t'=t. (B) Contours of MLWFs of penta-graphene with the C2-2p_z characteristics. (C) Contours of MLWFs of flat penta-graphene with the 2p_z characteristics.

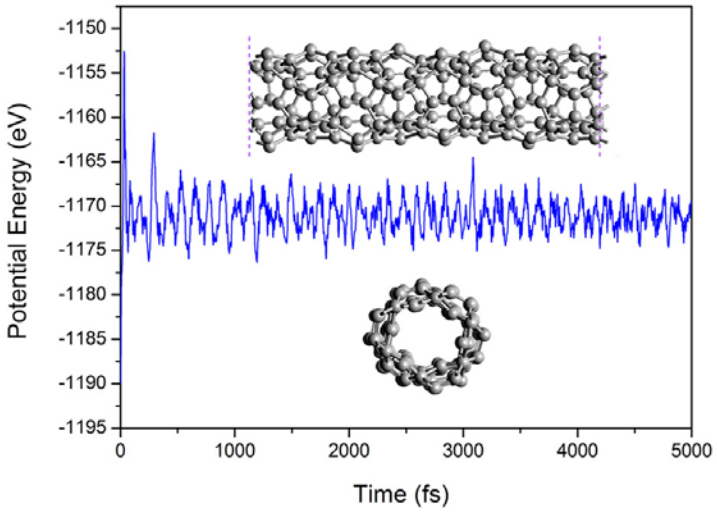

Fig. S7. Evolution of potential energy of (3, 3) penta-tube during AIMD simulations at 1000 K. 1×1×4 supercell is constructed for simulation to reduce the constraint of periodic condition in the axial direction. The insets show snapshots of atomic configuration at the end of the simulation.

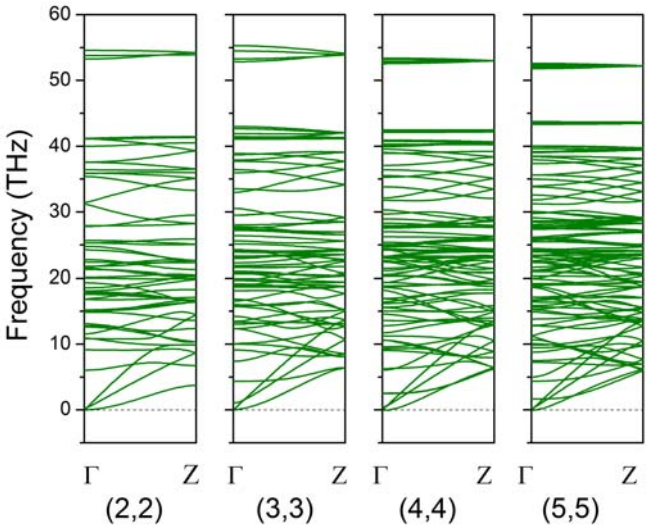

Fig. S8. Phonon spectra of penta-graphene-based nanotubes in different sizes: The high symmetric *q* point path is along the Γ (0, 0, 0) →Z (0, 0, 1/2) corresponding to the axial direction of nanotubes in the real space. The chiral vector number of each nanotube is denoted below the corresponding phonon spectra.

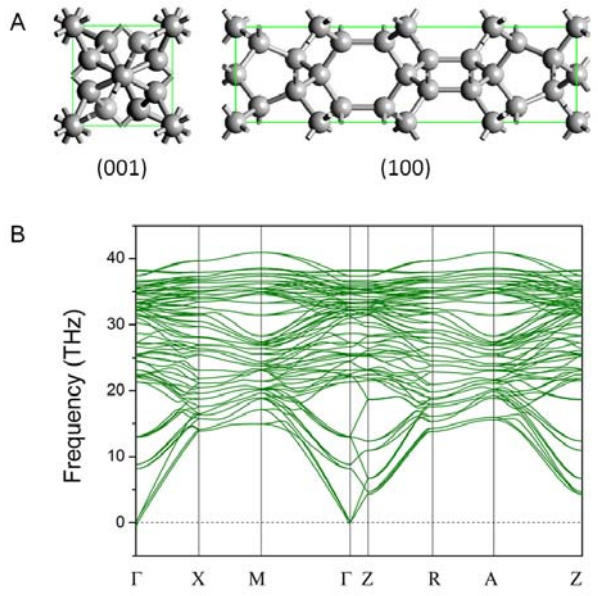

Fig. S9. 3D ABAA-T24 carbon phase derived from Penta-graphene. (A) Crystal structure and (B) phonon spectrum.

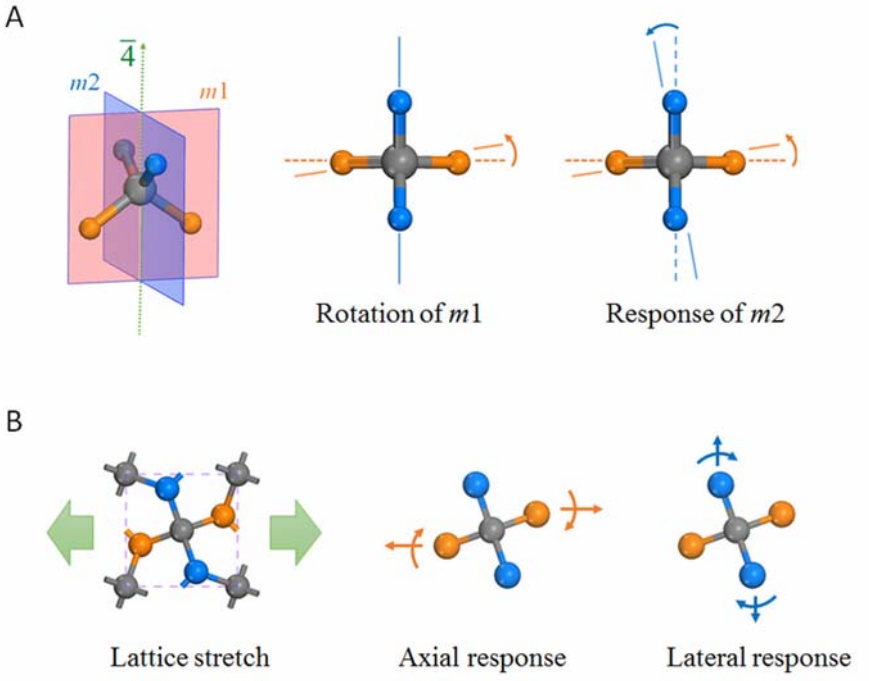

Fig. S10. Schematic illustration of the origin of auxetic behavior of penta-graphene. (A) The symmetric response in a CH_4 molecule. (B) Schematic illustration of the response of sp^2-hybridized C atoms in the penta-graphene unit cell when the lattice is uniaxially stretched. Arrows indicate the motion of atoms and rotation of the corresponding planes.

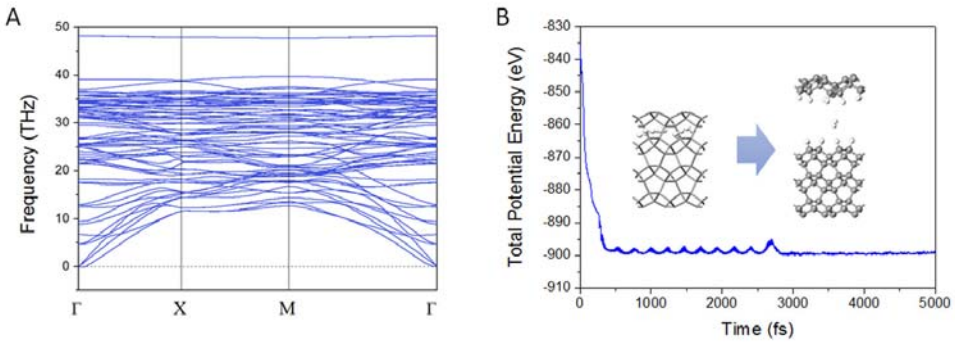

Fig. S11. (A) Phonon spectrum of a T12-carbon (001) thin film containing four penta-graphene layers. (B) Energy evolution of hydrogen intercalated T12-carbon thin film during AIMD simulations. The insets show the initial and final configurations.